Postprint of: Sawczak M., Sobaszek M., Siuzdak K., Ryl J., Bogdanowicz R., Darowicki K., Gazda M., Cenian A., Formation of Highly Conductive Boron-Doped Diamond on TiO_2 Nanotubes Composite for Supercapacitor or Energy Storage Devices, JOURNAL OF THE ELECTROCHEMICAL SOCIETY, Vol. 162, Iss. 10 (2015), pp. A2085-A2092

Formation of highly conductive boron-doped diamond on TiO_2 nanotubes composite for supercapacitor or energy storage devices

M. Sawczak[a], M. Sobaszek[b], K. Siuzdak[a], J. Ryl[c], R. Bogdanowicz[b], K. Darowicki[c], M. Gazda[d], and A. Cenian[a]*

[a]Polish Academy of Sciences, The Szewalski Institute of Fluid-Flow Machinery, 14 Fiszera St., 80-231 Gdańsk, Poland

[b]Department of Metrology and Optoelectronics, Faculty of Electronics, Telecommunications and Informatics, Gdańsk University of Technology, 11/12 G. Narutowicza St., 80-233 Gdańsk, Poland

[c]Department of Electrochemistry, Corrosion and Material Engineering, Faculty of Chemistry Gdańsk University of Technology, 11/12 G. Narutowicza St., 80-233 Gdańsk, Poland

[d]Department of Solid State Physics, Faculty of Applied Physics and Mathematics, Gdańsk University of Technology, 11/12 G. Narutowicza St., 80-233 Gdańsk, Poland

*Corresponding author: rbogdan@eti.pg.gda.pl, Phone: +48 58 347 1503, Fax: +48 58 347 18 48

In the present paper, we report the phenomena of the formation of the novel composite nanostructures based on TiO_2 nanotubes (NTs) over-grown by thin boron-doped diamond (BDD) film produced in Microwave Plasma Enhanced Chemical Vapor Deposition (PE MWCVD). The TiO_2 nanotube array overgrown by boron-doped diamond immersed in 0.1 M $NaNO_3$ can deliver high specific capacitance of 7.46 mF cm^{-2}. The composite electrodes were characterized by scanning electron microscopy (SEM), Raman spectroscopy, X-ray diffraction (XRD) and X-ray photoelectron spectroscopy (XPS) techniques. The depth-resolved investigations reveal that the primary anatase structure of TiO_2 NTs was partially transformed into Ti_2O_3 and non-stoichiometric TiC fractions. The explanation for this effect is the decomposing of TiO_2 NTs in the presence of activated hydrogen and carbon in the plasma leading to enhanced dehydration of NTs and carbon bonding originating from dissociated methane. This phenomena description fits also to processes demonstrated at hydrogenated TiO_2 (H-TiO_2) nanotube arrays used as electrode material for supercapacitors. Nevertheless, the increase of electrochemical performance can be attributed to several reasons: (1) the unique morphology of titania nanotubes and columnar BDD with intergrain defects and valley increasing specific area of electrode and (2) presence of TiC and Ti_2O_3 fractions introducing additional capacitance.

Introduction

Nowadays, the world is directed towards green energy and its efficient storage. Supercapacitors are notably useful due to the highly reversible charge storage process, long cycle-life and ability of rapid charging and discharging.[1] Presently, the supercapacitors are divided into two main types: electrical double layer capacitors (EDLC)[2] and redox supercapacitors (pseudocapacitors), followed by Faradic reactions carried out at the electrode material.[3] Moreover, they can store substantially more energy than conventional capacitors due to the very small distance of charge separation in the electrical double layer and highly extended surface area of electrode material.[4] EDLC provide far larger charging and discharging times than typical capacitors or batteries up to 10^{-6} s, charge/discharge efficiency close to ~100% and nearly infinite cycle-life.[4]

The titania nanotubes provide a large specific surface area, a direct pathway of charge transport but the specific capacitances are generally limited to less than 1 mF cm^{-2} without intentional doping or treatment. Lu and Li et al.[5,6] reported that hydrogenated TiO_2 by heating in hydrogen atmosphere resulted in an improvement of specific capacitance up to 3.24 mF cm^{-2}. Moreover, Wang and Leshuk et al.[7,8] received similar hydrogenated TiO_2 under hydrogen plasma treatment.

Recently, there is interest in synthesis of a different type of titania/carbon composite materials such as nanotubes,[9–12] and porous titanium carbides[13,14] which showed the enhanced effectiveness of those materials in photocatalysis,[15] electrochemical biosensing,[16] photoluminescence[17] and energy storage.[18,19]. Zhao et al.[9] prepared 5 mm long titanium oxide/carbon nanotube arrays by electrochemically coating the CNTs with a uniform layer of anatase TiO_2 nanoparticles. The obtained TiO_2/CNT showed fast photocurrent response and photocatalytic decomposition of organic substances. Chen and Dwivedi et al.[10,17] showed

synthesis of diamond like carbon (DLC) nanorods onto TiO_2/Ti nanotubes and DLC films on nanostructured titanium.

Yuan et al.[11,12] proposed a direct deposition of titania nanotubes onto boron-doped diamond (BDD) films by a liquid-phase deposition with ZnO nanorod arrays as the template. It was shown that BDD/TiO_2 structures have photoluminescence spectrum in a visible emission in a range of 550 – 750 nm, and also significant improvement of photoactivity. Vijayan et al.[15] coupled titania NTs and carbon NTs to create photocalytic nanocomposites. More recently, Gao et al.[18] have showed synthesis of MWNTs-TiO_2 hybrid electrode by a two-step method using (3-aminopropyl) triethoxysilane (APS) film chemisorbed on the surface of TiO_2 nanotubes. The MWNTs-TiO_2 nanotube electrode showed specific capacitance up to 4.4 mF cm^{-2} for 10 mg ml^{-1} of APS in 1 M H_2SO_4 and long-term cycle stability. Dash et al.[19] prepared titanium carbide derived nanoporous carbon by thermo-chemical etching of titanium carbide TiC in chlorine at a temperature range from 200 to 1200 ºC. Those electrodes showed specific up to 130 F g^{-1} in organic electrolyte with no degradation after 10 000 cycles.

It is worth noting that increasing capacitance is a synergetic effect of various factors like: combining different materials,[20] doping,[21] influence of plasma gas composition,[22] occurrence of pores and mesopores and their dimensions etc.[23] Chmiola et al.[23] reported the effect of pore size of carbide derived carbons (TiC) on specific capacitance. Smaller pore size and increasing the volume of pores result in an increase of specific capacitance.

Recently, we have investigated an enhanced electrochemical performance of composite TiO_2 NTs / BDD electrode. It was concluded that the BDD over-grown titania NTs can provide high capacitance mainly due to the following reasons: (i) substrate nucleation in nanodiamond slurry; (ii) influence of CH_4 : H_2 plasma treatment during initial stage of diamond film growing; (iii) high electrical conductivity BDD growth on top of nanotubes. These effects introduced a synergetic effect of specific capacitance increase resulting in 2.10,

4.79, and 7.46 mF cm^{-2} at a scan rate of 10 mV s^{-1} for the [B]/[C] ratio of 2, 5 and 10k, respectively.[24] However, the particular phenomena of enhanced electrochemical performance of composite TiO_2 NTs / BDD or hydrogenated TiO_2 (H-TiO_2) nanotube arrays has not yet been resolved and reported.

In this paper, we discuss the formation of TiO_2 NTs / BDD structure and effect of hydrogen plasma treatment of TiO_2 NTs. We resolve the potential origin of capacitive effect electric double layer supercapacitor based on TiO_2 nanotubes over-grown by thin boron-doped diamond film in microwave plasma assisted chemical vapor deposition process.

The advanced surface analysis was employed to investigate composite structure and its potential influence on the increase of capacitance. The scanning electron microscopy was applied to investigate evolution of surface morphology. Cross-sectional and depth-resolved composition of electrode was investigated by means of Raman spectroscopy and the electrode composition was analysed by means of X-ray photoelectron spectroscopy (XPS) and X-ray diffraction (XRD).

Experimental

Titania nanotube arrays were formed by anodization of 0.5 mm thick titanium foils (1 x 1 cm, ASTM Grade 1, 99.5%, Spinex, Poland). Before nanotube formation, titanium foil was ultrasonically cleaned in acetone, ethanol and water. Anodization took place in a two-electrode cell where Pt gauze served as a cathode and titanium substrate as anode. Electrodes were immersed in ethylene glycol solution containing 2% v/v of water and 0.3% wt NH_4F. Samples were anodized at electrode potential established at 60 V for 1 hour at 20°C and under continuous electrolyte stirring. After anodization, the samples were immersed in deionized water and dried on a hotplate at 80°C. Finally, the titania nanotube samples were annealed at 450°C for 1 h using a heating rate of 2 °C/min. in a tube furnace in oxygen atmosphere (in

order to remove organic residues from electrolyte) and allowed to cool gradually back to the ambient conditions.

The boron-doped diamond was synthesized in an MW PA CVD system (SEKI Technotron AX5400S, Japan) on titanium/titania nanotubes (NT) substrates (see Fig. 1). Substrates were seeded using seeding media of diamond suspension (DMSO/DND- 0.5% w/w) stabilized by polyvinyl alcohol (PVA) by means of spin-coating. Substrates were spun three times at 3000 rpm. During the deposition process, substrates were kept at 500°C. The excited plasma was ignited by microwave radiation (2.45 GHz). The plasma microwave power, optimized for diamond synthesis, was kept at 1300 W.[25,26] The molar ratio of CH_4-H_2 mixture was kept in this study at 4 % of gas volume at 200 sccm of total flow rate. The base pressure was about 10^{-6} Torr and the process pressure was kept at 50 Torr. The boron level expressed as [B]/[C] ratio in the gas phase was 10 000 ppm (BDD-10K). The diborane (B_2H_6) was used as dopant precursor. The growth time was 1 h, producing microcrystalline film of ca. 400 nm thickness.

Figure 1

The molecular structure of the electrode surface was analyzed using Raman technique. The Raman spectra were recorded at room temperature using micro-Raman system (InVia, Renishaw, UK) and 514 nm argon ion laser as excitation. The spectra were recorded in the range of 120 – 3300 cm^{-1}.

The surface morphology was analyzed with Scanning Electron Microscope (SEM) (EVO-40, Zeiss, Germany).

Electrochemical measurements of composite electrodes were performed by the potentiostat-galvanostat system AutoLab PGStat 302N in a standard three-electrode assembly at 295 K. Ti/TiO_2/BDD-10K films and as reference Ti/BDD and Ti/TiO_2 stayed as a working electrode. The counter electrode consisted of Pt gauze and reference electrode: Ag/AgCl/0.1 M KCl. Electrodes with a geometrical surface area of 1 cm^2 were tested by cyclic

voltammetry in solutions: 0.1 M $NaNO_3$ without and with 1 mM $K_3Fe(CN)_6$. Prior to taking electrochemical measurement, a pre-treatment was performed holding electrode at -0.1 V for 60 s.

The high-resolution photoelectron spectroscopy (ThermoFisher Scientific, Escalab 250Xi, UK) was used to determine chemical binding properties of the surface, utilizing monochromatic Al-Kα source with charge neutralization implemented by means of flood gun. High-resolution spectra were recorded at energy step size of 0.1 eV at a pass energy of 10 eV. Data analysis was performed using Avantage v.5 software provided by the manufacturer.

The samples were examined by X-ray diffractometer (Phillips X-Pert MPD, The Netherlands) employing Cu-Kα radiation (λ = 1.54178 Å). The XRD patterns were recorded with 2θ in range 20 – 70 by step scanning, using a fixed counting time of 2 s/step and 2θ increments of 0.02.

Results and discussion

Evolution of electrode surface morphology: The structure of composite electrode investigated using Scanning Electron Microscope (SEM) is presented in Figures 2 and 3. To visualize the inner structure of composite electrode the top BDD film was partially removed using laser ablation process (see Figure 2D). The laser ablation was carried out using Nd:YAG laser (1064 nm, 6 ns pulse duration) with top hat beam profile. The laser energy density was selected carefully to remove only the top BDD film without damaging the structure of titania nanotubes. Additionally, the cross-sectional SEM images were registered to visualise the internal structure of composite electrode (see Figure 3). The substrate for electrode preparation is formed by anodization of titanium foil resulting in the layer of TiO_2 nanotubes of 30 nm in diameter. The nanotubes have a regular continuous structure of 6 μm thickness as presented in Figure 2A. The TiO_2 NTs were overgrown in the MW PA CVD process with 400 nm thick BDD film. Figure 2C illustrates top view of composite electrode, while the cross-

sectional image is shown in Figure 3A. It could be observed in Figure 2B that the structure of TiO_2 NTs is not affected by BDD growth process and NTs keep their pristine shape.

Figure 2

This fact allows us to conclude that BDD nucleation kinetics is fast enough to create fully encapsulated film to prevent NTs etching effect by hydrogen species.

The polycrystalline BDD exhibits columnar growth. Thus, such films have highly tailorable microstructure and intergrain porosity.[27] They contribute to the increase of specific surface area and specific capacitance of composite electrode.[28]

Moreover, the high-resolution cross-sectional SEM microimages show semi-spherical nanostructures across TiO_2 NTs (Figure 3B). Thus, the TiO_2 NTs overgrown with BDD have been subjected to a detailed analysis using Raman spectroscopy, XRD and XPS to identify interface composition and origin of carbonous inclusions

Figure 3

Investigation of electrode composition by Raman spectroscopy: The micro-Raman analysis was preceded at the electrode cross section (see Figure 4) and at the surface of TiO_2 NTs after removing the top BDD film by laser ablation (see Figure 5). The depth profile Raman spectra were recorded at four depths starting from the electrode surface (depth 1) down to the titanium substrate foil (depth 4). Spectra recorded at the electrode surface (depth 1) confirmed the existence of typical BDD structure.[29] In the other profiles along the TiO_2 NTs (depths 2 – 4), only amorphous carbon structures were present at the side walls of NTs. The amount of carbon species decreases with the increasing of depth. This allows us to conclude that semi spherical nanoparticles observed along the side walls of TiO_2 NTs are formed by amorphous carbon structures. The Raman spectra registered in depths 2-4 reveal that primary anatase structure of TiO_2 NTs is transformed into another structure characterised with intense Raman bands located near 234 and 331 cm^{-1}, characteristic for Ti_2O_3.[30]

The Raman spectrum also exhibits broad signals centred around ~289 and 450 cm^{-1}, corresponding to Ti–O vibration modes in the titania framework.[31,32] Godbole et al.[31] observed that titanate nanotubes start disintegrating above $T_s \sim 500$ °C in HF CVD process, and exhibit different types of phase precipitation depending upon the temperature and gas atmosphere. Under appropriate conditions, the presence of activated hydrogen and carbon radicals leads to the formation of novel architectures of mixtures of nanophases such as carbide, or nonstoichiometric titania.

Figure 4

The spectra recorded at higher depths (e.g. depth 4) display the wide band with maximum at 605 cm^{-1}. This band could be assigned to a small volume of non-stoichiometric TiC fractions, which could be formed by the sudden temperature increase during the plasma ignition prior to the BDD growth process.[33] Moreover, this process is supported by nanoscale space confinement effect, the gas pressure in the nanotube is larger than that on the surface.[34] The nanotubular space provides a favourable nanoscale local environment with high pressure and temperature for enhancing the reaction of gaseous carbon species with TiO_2 NTs to form TiC.[35]

The decomposing of TiO_2 nanotubes in the presence of hydrogen was found to be more enhanced, possibly due to the presence of atomic hydrogen. The atomic hydrogen (activated due to the presence of microwaves) could react with H and OH within the nanotubes, leading to enhanced dehydration and hence collapsing of the tubes and carbon bonding.[31]

At depths 2-3, the strong Raman signals around ~1353 and 1600 cm^{-1} characteristic of sp^2-type bonded carbon in BDD coated TiO_2 NTs have been observed. The first band is attributed to the disordered carbon, which generally exhibit a second disorder-induced (D) band at 1350 cm^{-1}. It is associated with a double-resonance effect.[36] The second signal is assigned as the G

band corresponding to in-plane stretching at 1582 cm^{-1} of ordered graphite. The width and intensity of these two bands suggest the disordered nature of these carbon forms.

The G band shift to 1600 cm^{-1} indicates that graphite on the outermost surface of the nanotube consists of small sp^2 carbon clusters.[16] Additionally, the shift to 1353 and 1600 cm^{-1} in the TiO_2 NT/BDD composite, clearly indicates that the strong interaction between the NTs and the BDD could enhance charge transfer from the NTs to the BDD to separate and stabilize the charge and thereby hinder charge recombination.[15]

The insight into composition of plasma-processed NTs was carried out by means of Raman spectroscopy at laser ablated surface of composite electrode, where top BDD film was partially removed (see Figure 5C). As the reference, the original unprocessed TiO_2 NTs (see Figure 5A) and TiO_2 NTs treated in hydrogen plasma (Figure 5B) were additionally investigated. The second one was processed in pure hydrogen plasma (no admixture of CH_4), operating at similar conditions to that during CVD process, to avoid carbon inclusions. The Raman spectra presented in Figure 5B confirmed that during the plasma treatment the NTs are partially transformed into Ti_2O_3 with the corundum structure ($R\bar{3}c$ space group).[37]

Figure 5

Table 1

The weak band of anatase located near 139 cm^{-1} indicates incomplete transformation. The Raman bands characteristic of Ti_2O_3 are also identified for Ti_xO_y NTs in composite electrode (see Figure 5C). Moreover, the wide bands located at 420 and 605 cm^{-1} revealed the existence of TiC inside NTs structure. The shifts in band positions (Table 1) could be attributed to internal stresses in Ti_2O_3 crystalline structure induced by lattice defects generated by TiO_2 and TiC inclusions.

Investigation of electrode composition by means of XPS and XRD: Figure 6 presents high-resolution C1s spectra carried out for thin BDD film grown on TiO_2 NTs with 10k [B]/[C]

ratio XPS spectra contains 4 main peak components that were used for deconvolution of the spectra.

The main C1s peak, noted at 284.4 ± 0.2 eV, corresponds to hydrogen terminated boron doped diamond (HT-BDD).

Figure 6

The second peak is shifted of +0.7 eV and corresponds to oxygen terminated boron doped diamond (OT-BDD). The +1.2 eV shift of third peak is related to the presence of oxidized carbon atoms C-OH and C-OC. Finally, the weak peak observed at 283.4 eV is attributed to sp^2 hybridized carbon. Such interpretation is in agreement with previously published results by González-Elipe and Godbole et al. [38,39]

Table 2

As a result of BDD formation on top of TiO_2 NTs, the fourth component can be seen in Ti2p high-resolution spectra. It has been recognized as TiO, which was confirmed by both position (455.3 eV) as well as separation between Ti2p3 and Ti2p1 peaks.[40] It could be clearly observed that as a result of BDD layer growth or exposition to MW PA CVD, the structure of TiO_2 NTs changes and the oxidation level of titanium drops. A higher amount of Ti^{3+} and Ti^{2+} can be observed, together with a significant drop of Ti^{4+} and oxygen amounts in so treated TiO_2 NTs substrate.

The deconvolution of XPS spectrum performed at the cross-section of TiO_2 electrode reveals another peak, at considerably lower energy (454.6 eV), corresponding to TiC.[41] The presence of TiC was further confirmed with XRD analysis (see Figure 8). It is highly possible that this signal comes from semi-spherical nanostructures, observed in cross-sectional SEMs of TiO_2 NTs showed in Figure 3. These structures were not detected at the surface of NTs, due to limited depth of XPS measurements.

Figure 7

The XPS results shown in Table 3 revealed a decrease in the oxygen concentration with a simultaneous increase in the carbon content at the electrode cross-section. These variations in the state of the specimen can be explained on the basis of the simultaneous presence of activated hydrogen and carbon. Both of these can react with H and OH radicals bonded within the nanotubes[42] leading to disintegration of tubes, while, additionally, carbon can also react and replace bonded oxygen within the tube, since the available thermal energy is sufficient for such a reaction.

Table 3

Figure 8

In figure 8 the XRD patterns for the TiO_2 NTs before and after BDD deposition in CVD process are shown. The top pattern is characterized as anatase with a small amount of rutile crystalline phase that is typical for anodized titania calcined in 300 - 500˚C temperature range.[43] The bottom pattern which was registered for composite TiO_2 NTs / BDD electrode differs significantly from the pattern of the pristine TiO_2 NTs. Surprisingly, only very weak reflections belonging to anatase or rutile are observed in diamond overgrown NTs spectra (see Figure 8B). According to Kitada,[44] the XRD profile could be assigned to non-stoichiometric titanium oxide. Moreover, the BDD film overgrown NTs does not exhibit a multi-phase material nature. The authors believe that it is more likely that after the CVD process the NTs become the mixture of non- stoichiometric titanium oxide and other titanium compounds like Ti_2O_3 or TiC. Most of the registered peaks (marked as a blue x) are identified as rhombohedral Ti_2O_3 [JCPDS No 74-2278].[44] Similar signals were found for other suboxide samples reported by Siracusao et al.[45], Toyoda et al.[46] or Regoini et al.[47]

The signal marked as a red D, found at 44˚ is attributed to the (111) texture of CVD diamond.[48] Residual peaks registered at 35.9, 41.8 and 60.5˚ (marked as a green O) are

attributed to (111), (200) (220) titanium carbide khamrabeavite crystal planes, respectively [PDF No. 32-1283].[49,50]

Such a dramatic change of oxygen stoichiometry and, as a result, in crystal structure caused by BDD growth with preservation of nanotubular morphology was not yet observed for reduced TiO_2 nanotubes characterized with enhanced capacitance prepared by annealing in hydrogen atmosphere,[5] electrochemical hydrogenation doping process,[51] cathodic polarization[52] or achieved by melted Al reduction treating.[53]

Electrochemical performance of TiO_2/BDD electrode: Cyclic voltammetry was used to investigate the difference in electrochemical properties between composite material and its pure counterparts. Detailed analysis concerning influence of boron content in the gas phase during BDD grown process onto the electrochemical properties of the composite TiO_2-BDD material was given in our previous work.[24] As shown in Figure 9A, the CV shape is almost rectangular and no redox signal was observed as for typical double layer capacitance. The value of double layer capacitance was calculated based on the relation between the anodic current density at plateau j_a and the potential sweep rate formulated as $C_{dl} = j/v$. The specific areal capacitance for TiO_2/BDD-10k is 7.46 mF cm^{-2} whereas for pure TiO_2 it equals only 0.55 mF cm^{-2} and 0.11 mF cm^{-2} for BDD layer. The low capacitance reported for TiO_2 nanotubes[54] as well as for flat BDD layer[55] is typical for these kind of electrodes.

Additionally, the specific capacitance of BDD deposited onto the TiO_2 NTs was higher compared to self-doped TiO_2 (1.84 mF cm^{-2})[56], hydrogenated TiO_2 nanotubes (7.22 mF cm^{-2})[57], (3.24 mF cm^{-2})[58] or composite electrode materials such as BDD/carbon nanotubes[59] or BDD/carbon fibres[60] (1.94 mF cm^{-2}). Furthermore, when electrode layer thickness was taken into consideration, the volume capacitance for TiO_2/BDD equals 89 mF cm^{-3} that is meaningfully higher than gained for hydrogenated nanotubes (50 mF cm^{-3}) or BDD/carbon nanotube electrodes (4.7 mF cm^{-3}). It should be noted that such enhancement does not arise

from simple sum of capacitances for both counterparts but it should be related with other factors, such as chemical and morphology structure.

In order to investigate surface properties of BDD deposited onto the nanostructured and flat substrate, both electrodes were electrochemically tested in solution containing 1mM $K_3Fe(CN)_6$. Such ferro/ferricyanide redox system is characterized by inner-sphere electron transfer process with kinetics strongly related with density of electronic states near the formal potential or sp^2 bonded carbon. In Figure 9B, the cyclic voltammetry curves exhibit typical oxidation and reduction peaks that result from charge transfer at the electrode/electrolyte interface. For both electrode materials the degree of reversibility is almost the same that was probably caused by cathodic pretreatment at -0.1 V *vs*. Ag/AgCl/0.1M KCl for 1 min. However, in the case of composite electrode CV shape has characteristic charging current that is not observed for flat Ti/BDD layer. The better electrochemical performance of the as-prepared BDD-TiO_2 nanotube hybrid electrodes can be attributed to several reasons: (1) the unique morphology of titania nanotubes and columnar BDD with intergrain defects and valley increasing specific area in the hybrid electrode not only provide double-layer capacitance to the energy storage but also provide a more efficient conducting pathway for the diffusion of ions, resulting in fast electron transfer[61]; (2) changes in the titania chemical structure caused by BDD growth during CVD process e.g. TiC bonding can increase the contact between BDD and tubular structure of TiO_2 and introduce additional capacitance.[18,62]

Concerning the type of substrate used for BDD grown, application of titania nanotube arrays results in increased real surface area providing higher boundary density in comparison to flat plate,[63,64] e.g. Ti metal plate. As it was shown in the SEM images, BDD crystals form very tight layer onto the TiO_2 substrate as well as in any other available free space, e.g. titania side walls.

Figure 9

Therefore, electrode/electrolyte interface available for charge accumulation is highly improved and capacitive current remarkably increases. Furthermore, the specific architecture of titania allows a direct electron transfer along the tube channel that was considered to be crucial for capacitance properties.[65]

Additionally, XRD, XPS and Raman spectroscopy techniques allowed for more detailed material characterization. According to the described results, the chemical structure of NTs underwent dramatic modification: instead of pure anatase phase in composite material: rutile, titanium carbide and non-stochiometric oxide with substantial amount of Ti^{3+} arises. In terms of electrical conductivity, anatase is much more conductive than amorphous TiO_2, and the presence of rutile may lead to a decrease in electrical conductivity.[66] However, according to Zhou,[67] the mixture of rutile and anatase phases was assumed to be capable to exhibit higher capacitance than a single anatase phase. As it was generally reported by Salari et al.,[68] the presence of rutile phase gives higher conductivity and lower charge transfer limitations that is attributed to the consumption of Ti^{4+} and the simultaneous increase of Ti^{3+}/Ti^{4+} within the TiO_2 network. With the decreasing O/Ti ratio that is equivalent to increasing deviation from the oxygen stoichiometry, TiO_{2-y} the layer become more conductive. The close relation between the electrical resistivity and y indicates that oxygen non-stoichiometry is the source of electrons in the conduction band of titanium dioxide film. It leads to higher ionic transfer during charge and discharge processes, and consequently results in higher capacitance values.

The presence of a small amount of titanium carbide should not be ignored as well. Its presence was confirmed on XPS spectra registered at the cross-section of composite materials, using XRD and Raman spectroscopy technique. TiC is a typical transition metal carbide held together with, ionic, covalent and metallic bond. It is characterized by high thermostability, high strength and hardness, toughness and electrical conductivity.[69] The presence of TiC significantly improves composite material electric conductivity[70] as well as capacitance.[52]

There are known nanoporous TiC-TiO_2 systems characterized by highly enhanced capacitance in comparison to pure TiC.[71] Thus, the carbide formed within titania tubular structure could have also powerful impact on the overall TiO_2/BDD composite electrochemical performance.

Conclusions

The formation process of the composite nanostructures based on TiO_2 nanotubes (NTs) over-grown by thin boron-doped diamond film in PE MWCVD was investigated in details. The cross-sectional and depth-resolved studies reveal that primary anatase structure of TiO_2 NTs was partially transformed into Ti_2O_3 and non-stoichiometric TiC fractions. This phenomenon is attributed to the simultaneous presence of activated hydrogen and carbon in the plasma leading to enhanced dehydration of NTs followed by carbon bonding.

Moreover, the enhanced capacitive effect of TiO_2 NT / BDD could be recognized as: (1) the unique synergistic morphology of NTs and BDD providing more efficient conducting pathway for the diffusion of ions and (2) partial decomposition of NTs and transformation towards to TiC and Ti_2O_3 fractions.

Variation of the electrochemical properties of NTs has been already achieved by electrochemical reduction process, hydrogen plasma treatment or annealing in an inert atmosphere providing higher conductivity due to Ti^{4+} to Ti^{3+} conversion and TiC formation. Despite TiO_2 NT / BDD were characterized with improved capacitance comparing to pristine TiO_2 nanotubes, their Raman spectra as well as XRD pattern does not change significantly upon modification as it take place for BDD overgrown TiO_2 NTs. Thus, the proposed synthesis procedure leads to the formation of composite materials that surface and chemical structure highly deviates from its pure counterparts. Furthermore, electrochemical and physicochemical studies showed that TiO_2 NT / BDD electrodes could be regarded as promising materials for supercapacitor or energy storage devices.

Acknowledgements

The authors gratefully acknowledge financial support from the Polish National Science Centre (NCN) under Grant No. 2011/03/D/ST7/03541 and No. 2012/07/D/ST5/02269. The DS funds of the Faculty of Electronics, Telecommunications and Informatics of the Gdansk University of Technology are also acknowledged.

Notes and references

1. A. K. Shukla, *Resonance*, **6**, 72–81 (2001).

2. P. Simon and Y. Gogotsi, *Nat. Mater.*, **7**, 845–854 (2008).

3. X. Lang, A. Hirata, T. Fujita, and M. Chen, *Nat. Nanotechnol.*, **6**, 232–236 (2011).

4. A. G. Pandolfo and A. F. Hollenkamp, *J. Power Sources*, **157**, 11–27 (2006).

5. X. Lu et al., *Nano Lett.*, **12**, 1690–1696 (2012).

6. S.-C. Li et al., *J. Am. Chem. Soc.*, **130**, 9080–9088 (2008).

7. Z. Wang et al., *Adv. Funct. Mater.*, **23**, 5444–5450 (2013).

8. T. Leshuk et al., *ACS Appl. Mater. Interfaces*, **5**, 1892–1895 (2013).

9. Y. Zhao et al., *Nanotechnology*, **21**, 505702 (2010).

10. J.-B. Chen et al., *Appl. Surf. Sci.*, **256**, 39–42 (2009).

11. J. Yuan et al., *Chem. Res. Chin. Univ.*, **30**, 18–22 (2014).

12. J. Yuan, H. Li, S. Gao, Y. Lin, and H. Li, *Chem. Commun.*, **46**, 3119–3121 (2010).

13. M. R. Lukatskaya et al., *Science*, **341**, 1502–1505 (2013).

14. A. Parker, M. Marszewski, and M. Jaroniec, *ACS Appl. Mater. Interfaces*, **5**, 1948–1954 (2013).

15. B. K. Vijayan, N. M. Dimitrijevic, D. Finkelstein-Shapiro, J. Wu, and K. A. Gray, *ACS Catal.*, **2**, 223–229 (2012).

16. L. Hu et al., *Anal. Chem.*, **83**, 8138–8144 (2011).

17. N. Dwivedi, S. Kumar, and H. K. Malik, *ACS Appl. Mater. Interfaces*, **3**, 4268–4278 (2011).

18. Z. Gao et al., *J. Power Sources*, **283**, 397–407 (2015).

19. R. Dash et al., *Carbon*, **44**, 2489–2497 (2006).

20. S. Chen, J. Zhu, X. Wu, Q. Han, and X. Wang, *ACS Nano*, **4**, 2822–2830 (2010).

21. H. Wu et al., *Electrochimica Acta*, **116**, 129–136 (2014).

22. G. Lota, J. Tyczkowski, R. Kapica, K. Lota, and E. Frackowiak, *J. Power Sources*, **195**, 7535–7539 (2010).

23. J. Chmiola, G. Yushin, R. Dash, and Y. Gogotsi, *J. Power Sources*, **158**, 765–772 (2006).

24. K. Siuzdak, R. Bogdanowicz, M. Sawczak, and M. Sobaszek, *Nanoscale*, **7**, 551–558 (2014).

25. R. Bogdanowicz, *Metrol. Meas. Syst.*, **21**, 685–698 (2014).

26. M. Sobaszek et al., *Opt. Mater.*, **42**, 24–34 (2015).

27. Y.-G. Lu et al., *Appl. Phys. Lett.*, **101**, 041907 (2012).

28. J. Chmiola, G. Yushin, R. Dash, and Y. Gogotsi, *J. Power Sources*, **158**, 765–772 (2006).

29. R. Bogdanowicz et al., *Diam. Relat. Mater.*, **39**, 82–88 (2013).

30. Y. Chen and J. Mao, *J. Mater. Sci. Mater. Electron.*, **25**, 1284–1288 (2014).

31. V. P. Godbole et al., *Nanotechnology*, **16**, 1186 (2005).

32. X. Sun and Y. Li, *Chem. – Eur. J.*, **9**, 2229–2238 (2003).

33. B. H. Lohse, A. Calka, and D. Wexler, *J. Alloys Compd.*, **434–435**, 405–409 (2007).

34. X. Pan et al., *Nat. Mater.*, **6**, 507–511 (2007).

35. V. K. Varadan, R. D. Hollinger, V. V. Varadan, J. Xie, and P. K. Sharma, *Smart Mater. Struct.*, **9**, 413 (2000).

36. A. C. Ferrari and J. Robertson, *Phys. Rev. B*, **61**, 14095–14107 (2000).

37. S. V. Ovsyannikov et al., *J. Phys. Condens. Matter*, **22**, 375402 (2010).

38. J. Ryl, R. Bogdanowicz, P. Slepski, M. Sobaszek, and K. Darowicki, *J. Electrochem. Soc.*, **161**, H359–H364 (2014).

39. V. P. Godbole et al., *Nanotechnology*, **16**, 1186 (2005).

40. A. R. González-Elipe, G. Munuera, J. P. Espinos, and J. M. Sanz, *Surf. Sci.*, **220**, 368–380 (1989).

41. Y. Cheng and Y. F. Zheng, *Surf. Coat. Technol.*, **201**, 4909–4912 (2007).

42. S. Zhang et al., *J. Solid State Chem.*, **177**, 1365–1371 (2004).

43. K. Lee, D. Kim, and P. Schmuki, *Chem. Commun.*, **47**, 5789–5791 (2011).

44. A. Kitada et al., *J. Am. Chem. Soc.*, **134**, 10894–10898 (2012).

45. S. Siracusano, V. Baglio, C. D'Urso, V. Antonucci, and A. S. Aricò, *Electrochimica Acta*, **54**, 6292–6299 (2009).

46. L. R. Radovic, Ed., *Chemistry & Physics of Carbon: Volume 31*, 1 edition., p. 297, CRC Press, New York, (2012).

47. D. Regonini, A. C. E. Dent, C. R. Bowen, S. R. Pennock, and J. Taylor, *Mater. Lett.*, **65**, 3590–3592 (2011).

48. L. R. Radovic, Ed., *Chemistry & Physics of Carbon: Volume 31*, 1 edition., p. 297, CRC Press, New York, (2012).

49. D. Gu, Y. Lu, B. Yang, and Y. Hu, *Chem. Commun.*, 2453–2455 (2008).

50. J. Zhang, J. W. Zimmer, R. T. Howe, and R. Maboudian, *Diam. Relat. Mater.*, **17**, 23–28 (2008).

51. H. Wu et al., *Electrochimica Acta*, **116**, 129–136 (2014).

52. H. Zhou and Y. Zhang, *J. Phys. Chem. C*, **118**, 5626–5636 (2014).

53. H. Cui et al., *J. Mater. Chem. A*, **2**, 8612–8616 (2014).

54. Y. Xie, L. Zhou, C. Huang, H. Huang, and J. Lu, *Electrochimica Acta*, **53**, 3643–3649 (2008).

55. H. Zanin et al., *ACS Appl. Mater. Interfaces*, **6**, 990–995 (2014).

56. H. Zhou and Y. Zhang, *J. Phys. Chem. C*, **118**, 5626–5636 (2014).

57. H. Wu et al., *Nanotechnology*, **24**, 455401 (2013).

58. X. Lu et al., *Nano Lett.*, **12**, 1690–1696 (2012).

59. H. Zanin et al., *ACS Appl. Mater. Interfaces*, **6**, 990–995 (2014).

60. E. C. Almeida, M. R. Baldan, J. M. Rosolen, and N. G. Ferreira, *Diam. Relat. Mater.*, **17**, 1529–1533 (2008).

61. D. P. Dubal, G. S. Gund, C. D. Lokhande, and R. Holze, *ACS Appl. Mater. Interfaces*, **5**, 2446–2454 (2013).

62. Z. Jin et al., *Nanotechnology*, **25**, 395401 (2014).

63. N. G. Ferreira et al., *Diam. Relat. Mater.*, **14**, 441–445 (2005).

64. A. V. Diniz, N. G. Ferreira, E. J. Corat, and V. J. Trava-Airoldi, *Mater. Res.*, **6**, 57–61 (2003).

65. M. Salari, S. H. Aboutalebi, K. Konstantinov, and H. K. Liu, *Phys. Chem. Chem. Phys.*, **13**, 5038–5041 (2011).

66. H.-T. Fang et al., *Nanotechnology*, **20**, 225701 (2009).

67. M. Zhou, A. M. Glushenkov, O. Kartachova, Y. Li, and Y. Chen, *J. Electrochem. Soc.*, **162**, A5065–A5069 (2015).

68. M. Salari, S. H. Aboutalebi, K. Konstantinov, and H. K. Liu, *Phys. Chem. Chem. Phys.*, **13**, 5038–5041 (2011).

69. D. Zhang, J. Li, and J. Zheng, *Mater. Lett.*, **93**, 99–102 (2013).

70. Y.-T. Weng, H.-A. Pan, N.-L. Wu, and G. Z. Chen, *J. Power Sources*, **274**, 1118–1125 (2015).

71. M. Arulepp et al., *J. Power Sources*, **162**, 1460–1466 (2006).

Table 1 Raman bands positions for unprocessed and plasma processed TiO_2 NTs.

(a) – TiO_2 NTs	**(b) – Ti_xO_y NTs in H_2 plasma**	**(c) – Ti_xO_y NTs overgrown by BDD film**	**Peak assignment**
143.7	139	150.9	TiO_2
-	209.7	208.3	Ti_2O_3
-	274	243.6	Ti_2O_3
-	300.9	289	Ti_2O_3
-	340.6	331.8	Ti_2O_3
396.6	-	-	TiO_2
-	-	420	TiC
-	455.3	-	Ti_2O_3
-	506.7	495	Ti_2O_3
518.6	-	-	TiO_2
-	558.2	553.8	Ti_2O_3
-	-	605	TiC
637.7	-	-	TiO_2
-	-	1353	Carbon – D-peak
-	-	1600	Carbon – G-peak

Table 2. Percentage contribution (in at.%) of each C1s peak for BDD grown on TiO_2 NTs with 10k [B]/[C] ratio.

Name	**Peak BE [eV]**	**10k BDD [at.%]**
C-C $_{HT\text{-}BDD}$	284.5	53.8
C-C $_{OT\text{-}BDD}$	285.2	25.4
C-O	285.7	18.4
C-C $_{sp2}$	283.4	1.7

Table. 3 Percentage contribution (in at.%) of Ti2p3 peaks for TiO_2 NTs substrate reference sample and structure change as a result of BDD film growth.

	Name	Peak BE [eV]	Separation [eV]	Reference [at.%]	Under BDD [at.%]	Cross-section [at.%]
Ti2p3	TiO_2 anatase	459.1	5.8	17.2	21.5	24.2
Ti2p3	TiO_2 rutile	458.6	5.6	12.2	5.7	6.4
Ti2p3	Ti_2O_3	457.2	5.4	3.7	4.7	3.3
Ti2p3	TiO	455.4	4.6	--	2.2	--
Ti2p3	TiC	454.6	6.0	--	--	3.3
O1s	TiO_2, Ti_2O_3	530.4	--	66.9	65.9	62.8

Figure 1

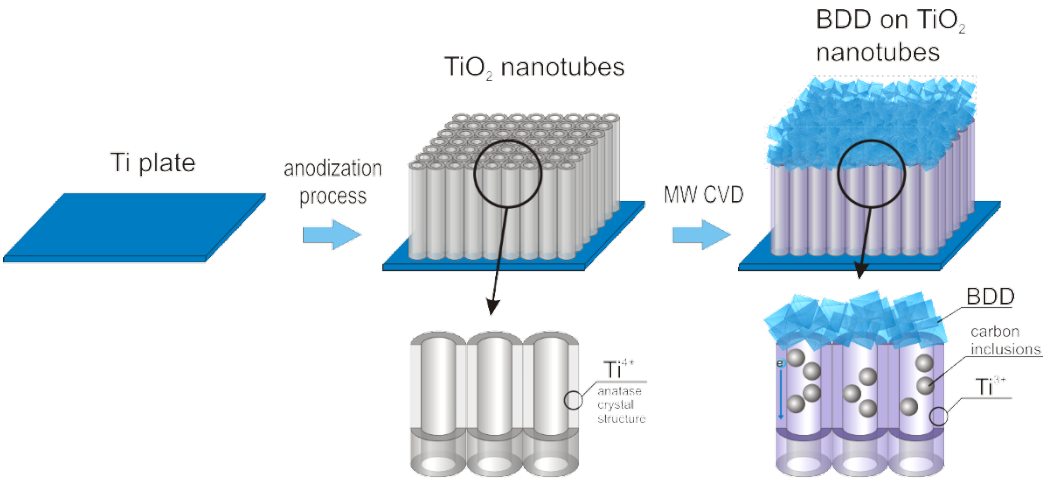

Figure 2

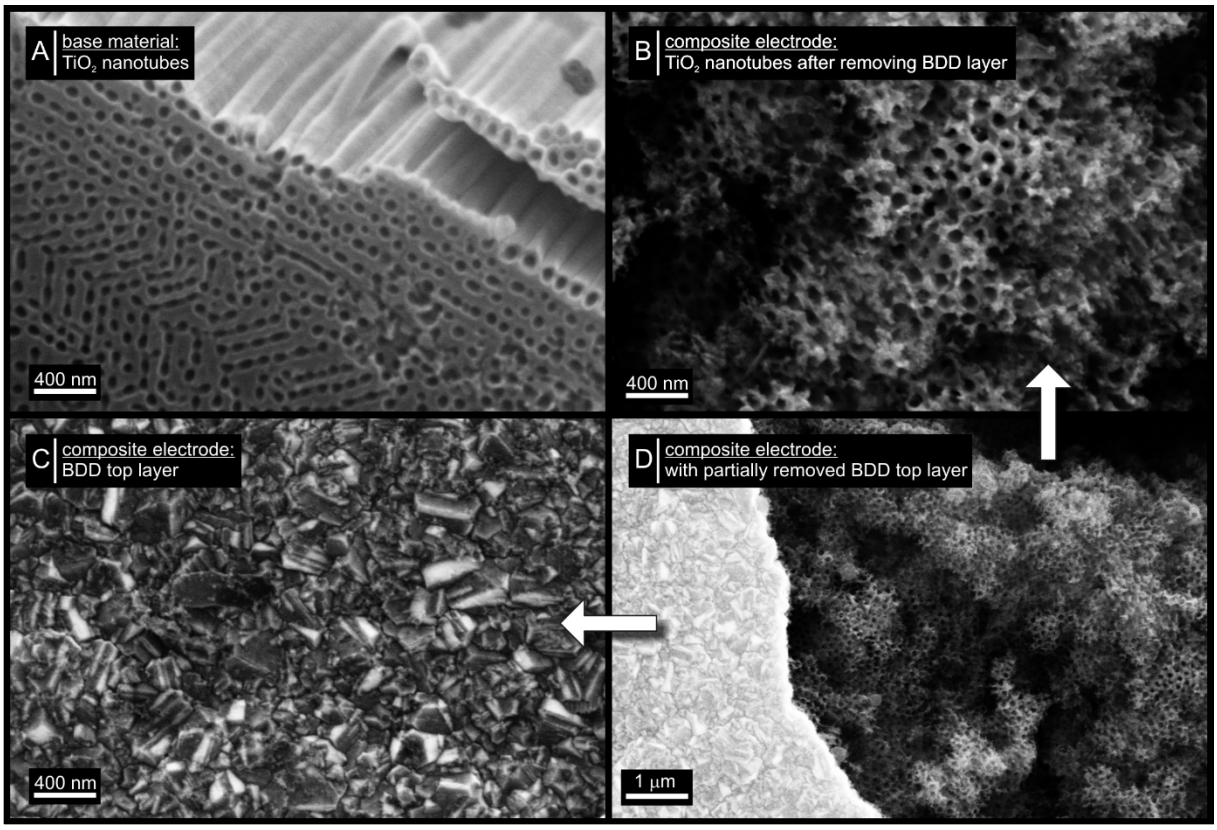

Figure 3

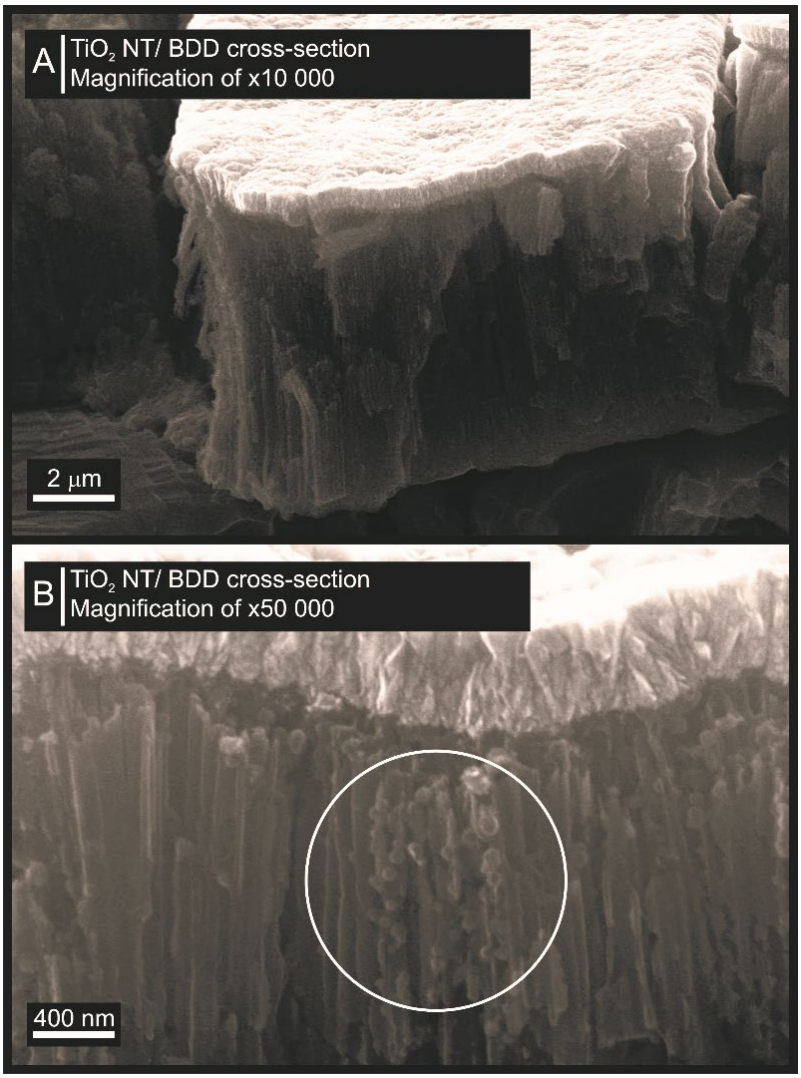

Figure 4

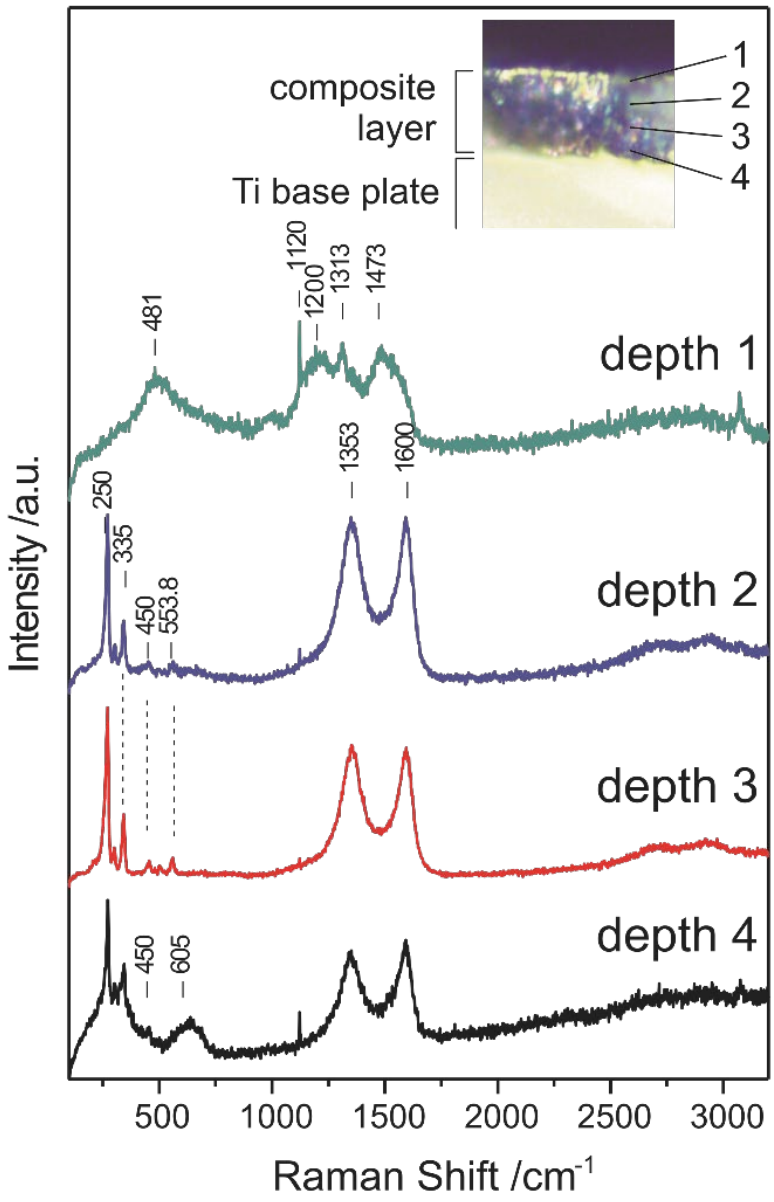

Figure 5

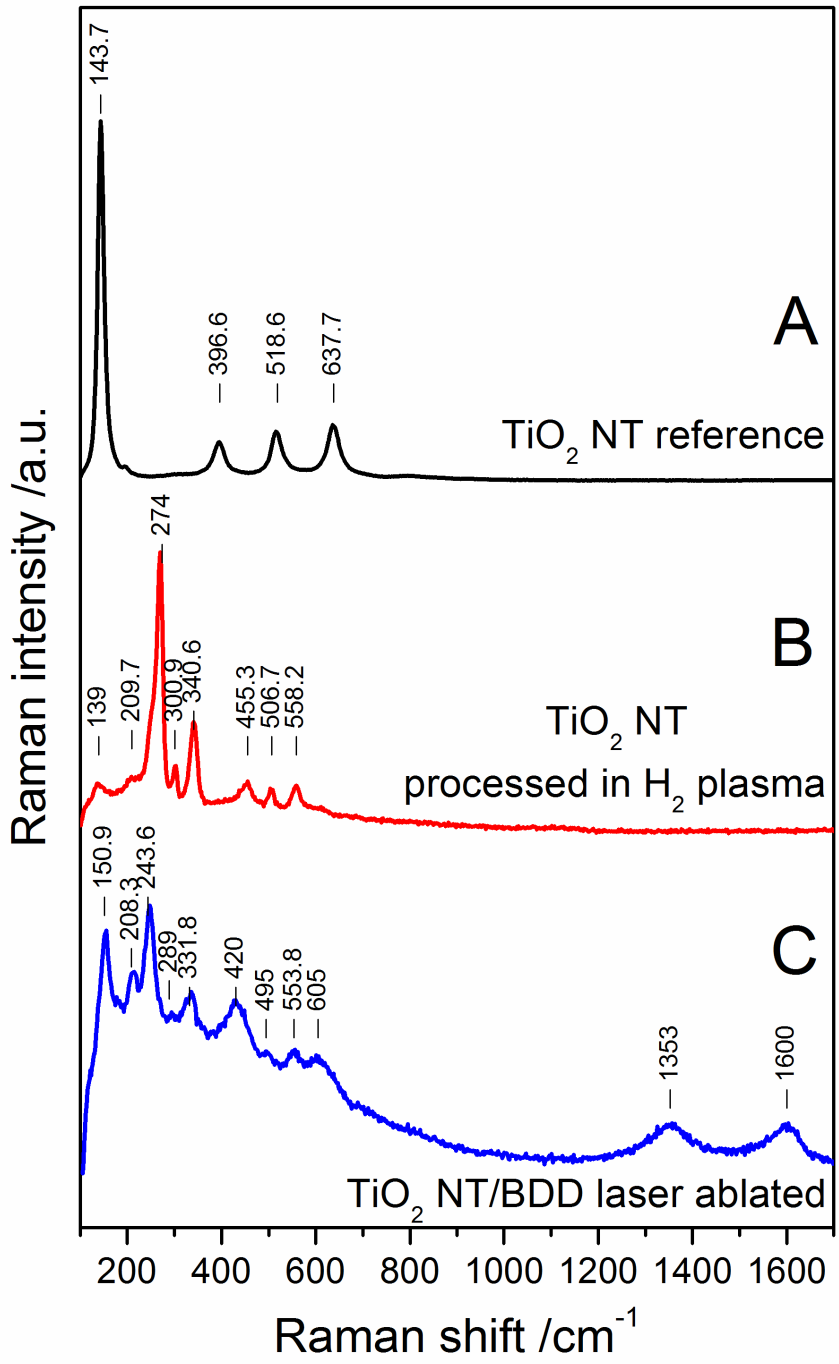

Figure 6

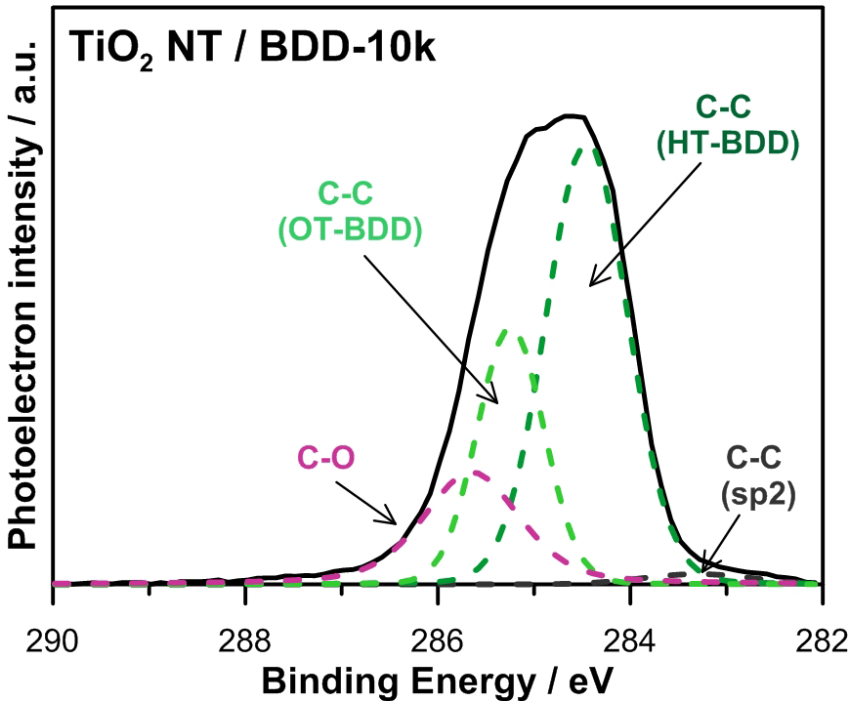

Figure 7

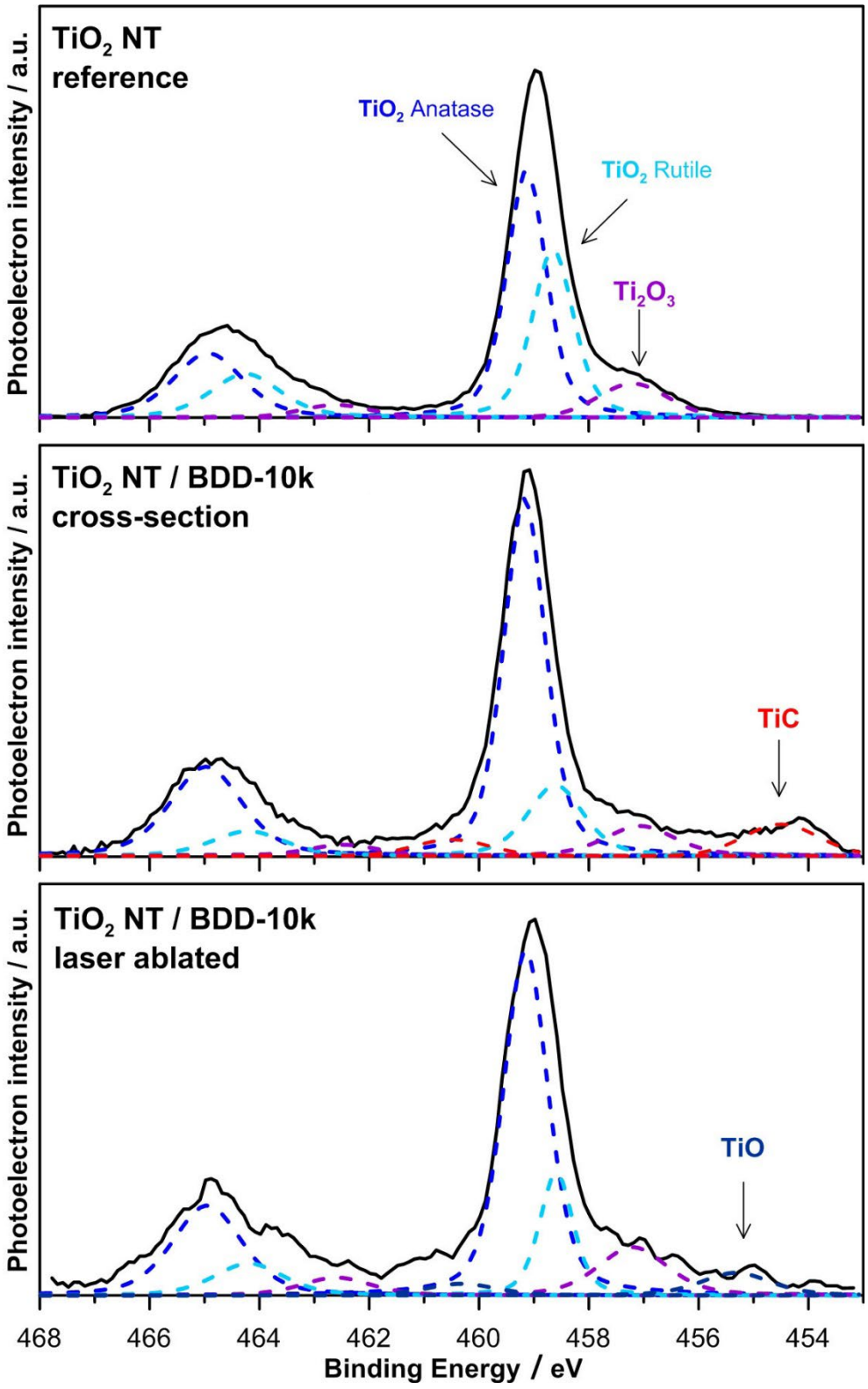

Figure 8

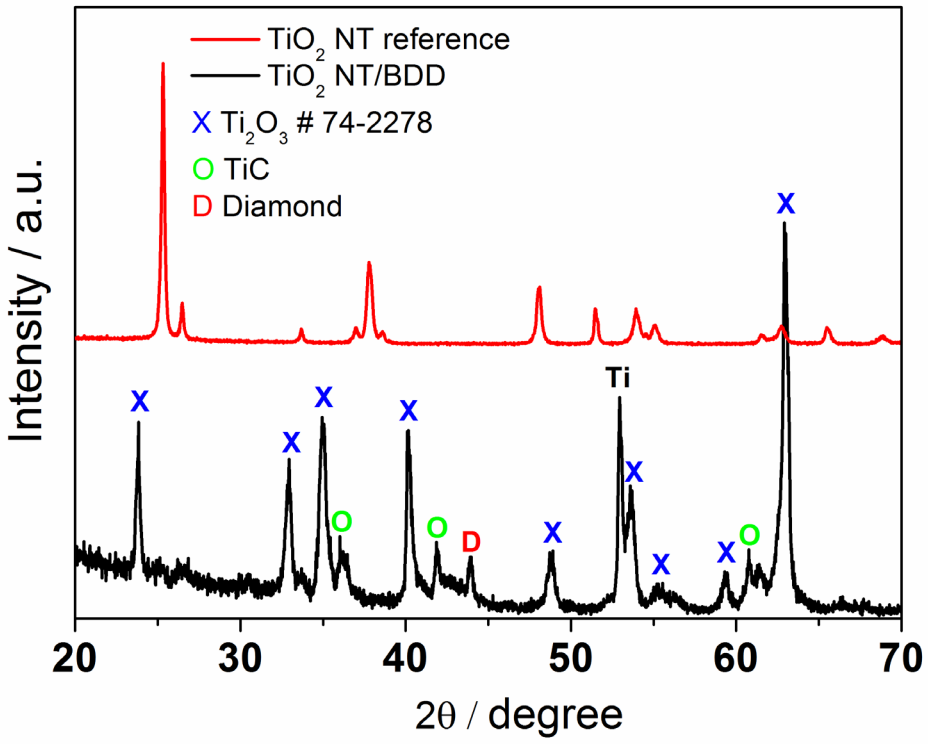

Figure 9

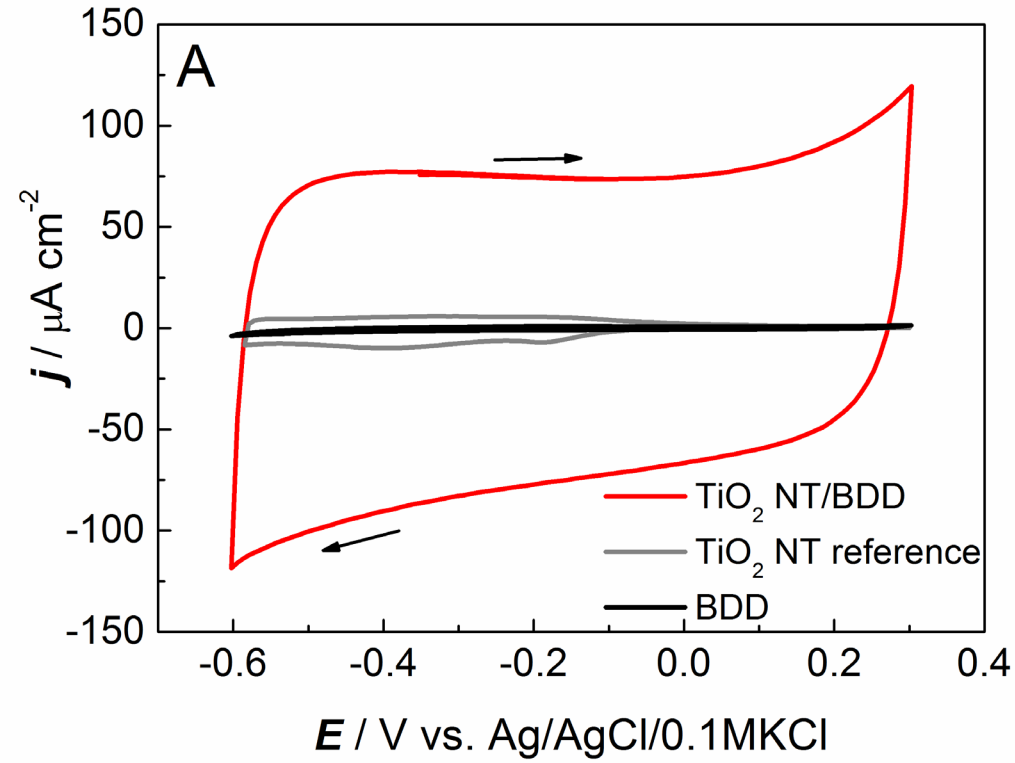

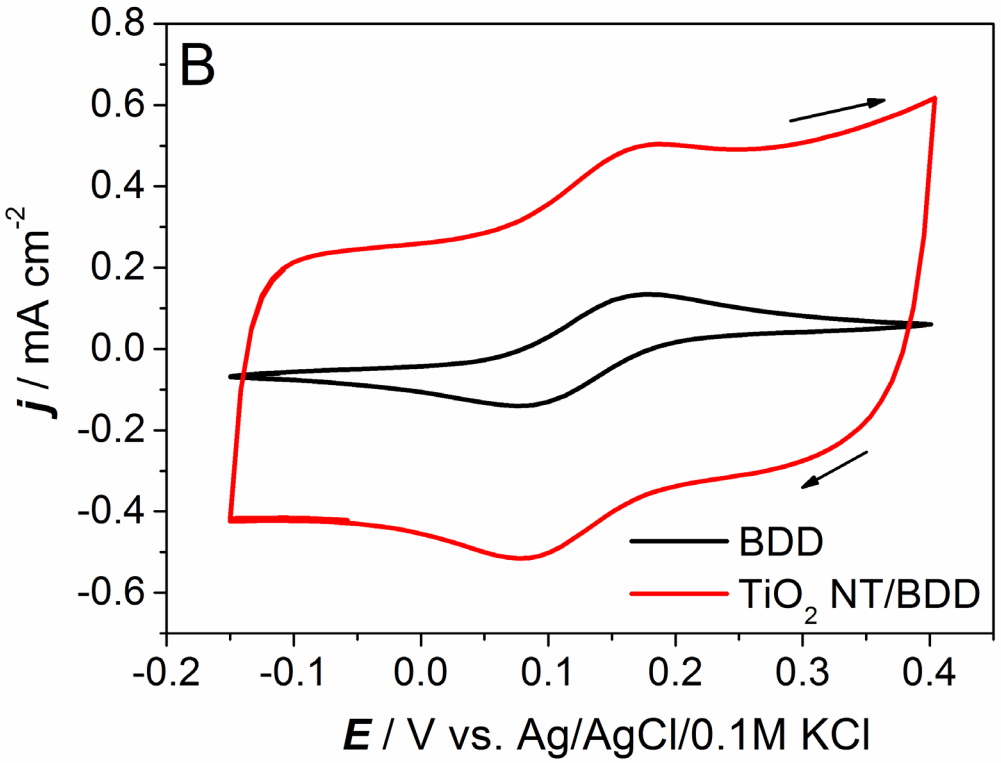

Figure 1. Formation scheme of composite TiO_2 nanotubes / boron-doped diamond electrode.

Figure 2. SEM images of TiO_2 NTs before deposition of BDD film (A) and composite nanostructure in details: surface of Ti_xO_y NTs located below BDD film (B); BDD surface (C) and composite electrode with partially removed BDD film using laser ablation (D).

Figure 3. Various zooms of cross-sectional SEM images of composite TiO_2 NTs / BDD electrode: (A) magnification of 10 000x; (B) magnification of 50 000x.

Figure 4. The Raman spectra recorded at the cross section of composite TiO_2 NTs / BDD electrode obtained at four depths.

Figure 5. Raman spectra of unprocessed and plasma processed TiO_2 NTs; (a) unprocessed TiO_2 NTs given for reference, (b) NTs processed in the pure hydrogen plasma (no admixture of CH_4) and (c) NTs overgrown by BDD film recorded after removing BDD top layer in laser ablation process.

Figure 6. The high-resolution C1s spectra carried out for thin BDD film grown on TiO_2 NTs with 10k [B]/[C] ratio.

Figure 7. The evolution of Ti2p high-resolution spectra of plasma processed TiO_2 NTs. The unprocessed TiO_2 NTs were given for reference (top plot).

Figure 8. The XRD patterns for the TiO_2 NTs before and after BDD deposition in CVD process: x – Ti_2O_3, O - TiC, D- diamond.

Figure 9. Cyclic voltammetry curves: (a) the composite electrodes TiO_2 NTs / BDD-10k, pure titania and BDD layer immersed in 0.1 M $NaNO_3$ (ν = 10 mV/s), (b) the BDD and the TiO_2 NTs / BDD electrodes in 1 mM $K_3(FeCN)_6$/0.1M $NaNO_3$ (ν = 10 mV/s).